Chapter 3
Optical Properties of Metal, Semiconductor and Ceramic Nanostructures Grown by Liquid Phase-Pulsed Laser Ablation

P. M. Aneesh and M. K. Jayaraj

1 Introduction

Nanostructured materials have gained extensive research interest in the last few decades owing to its exceptional chemical, optical, electronic and magnetic properties different from their bulk counterparts. In last few decades, extensive researches were carried out in the synthesis of colloidal nanoparticles because of their versatile properties promising for application in various fields like drug delivery [1, 2], imaging [3–6], diagnostics [7–10] and for the growth of nanocomposites with peculiar optical, mechanical or bioactive properties [11–14]. Pulsed laser ablation (PLA) was first developed as technique for the growth of thin films in the 1960s, shortly after the invention of the pulsed ruby laser. Since then, the growth of thin films by laser ablation in vacuum and in various gases ambient has been studied by many researchers. Wide variety of thin films of high-temperature superconductors [15, 16], metals, semiconductors, oxides, diamond-like carbon [17, 18] and other ceramics [19, 20] can be deposited using different target materials and gaseous atmosphere, and varying parameters such as the laser fluence, laser wavelength and pulse duration.

Pulsed laser ablation is considered as the promising and most flexible technique because almost all kinds of materials can be ablated at ultra-high-energy density. The process parameters like irradiation time, energy density, wavelength, etc. during the growth process can be controlled very easily [21, 22]. Patil and co-workers in 1987 first reported the pulsed laser ablation on solid–liquid interface by ablating a pure iron target in water to form iron oxides with metastable phases using pulsed laser

P. M. Aneesh (✉)
Department of Physics, Central University of Kerala, Tejaswini Hills, Periye, Kasaragod, Kerala 671320, India
e-mail: aneeshpm@cukerala.ac.in

M. K. Jayaraj
Department of Physics, Cochin University of Science and Technology, Kochi 682022, India

M. K. Jayaraj (ed.), *Nanostructured Metal Oxides and Devices*,
Materials Horizons: From Nature to Nanomaterials,
https://doi.org/10.1007/978-981-15-3314-3_3

beam [23]. This method is known as liquid phase-pulsed laser ablation (LP-PLA), and the laser beam is focused on the solid target surface through the liquid. This pioneering work based on PLA of solids in various liquids opened new routes for the synthesis of materials and LP-PLA method has been used to produce a wide variety of novel materials, such as metallic nanocrystals, nanodiamond and related nanocrystals, nanocrystal alloys and metal oxides with peculiar properties.

LP-PLA techniques have become a promising and versatile growth technique for nanostructures that allows one to choose suitable solid targets and confining liquids. LP-PLA technique has many advantages over the other conventional physical methods such as pulsed laser ablation in vacuum, sputtering and evaporation and chemical methods such as sol–gel and co-precipitation. It is a chemically simple and clean synthesis process. One of the advantages of LP-PLA technique is that since the final product is usually obtained without any by-products and hence further purification is not required. The other advantage of this technique is that it requires only inexpensive equipment for controlling the ablation atmosphere, and the parameters can be controlled very easily. Also, the amount of chemical quantity required for synthesis is minimum as compared to the other conventional chemical process. The extreme confined conditions, induced high temperature and pressure region during the processes, favor the formation of metastable phases. Thus, nanostructures of metals and semiconductors can be easily synthesized by this technique.

Commercially available colloids are usually synthesized by sol–gel or salt precipitation processes, and in these processes precursor, additive and surfactant systems need to be designed for each type of nanoparticles. Metal acetates and carbonates are the commonly used chemical precursors for every synthesis process in nanochemistry. Oxidation of metal and hydroxylations of ceramic samples are the other drawbacks of these kinds of synthesis techniques. The unreacted precursors and substituents get agglomerated and remain as sediments in the final colloidal product [24]. These days, large endeavors are being made for an efficient and systematic purification and removal of these contaminants [25].

Regardless of the advancement in the field of wet chemistry, the potential of sol–gel chemistry, particularly product diversity, have not been utilized adequately [26]. Furthermore, the products are often constricted to thermodynamically stable crystal structures, as a result of which the fabrication of hard ceramics like alpha aluminum oxide and tetragonal zirconium dioxide becomes complicated. Also, as the required forces increase exponentially with smaller particle size, it is not possible to form nanoparticles from these hard materials by mechanical milling. Likewise, milling processes may introduce contaminants from grinding media [27]. But the development and growth of new nanomaterials with LP-PLA technique require comparably little effort. The limitations of LP-PLA technique are the low yield that is mostly restricted to about (0.01–0.1) μg/min [28], and there are knowledge deficits on the physical and chemical processes involved.

LP-PLA technique involves focusing a high-power laser beam onto the surface of a solid target, which is submerged in a liquid. During this process, the interaction of laser beam with the surface of target leads to vaporization of surface and generates an ablation plume, which contains many species such as atoms, clusters and ions, rushing

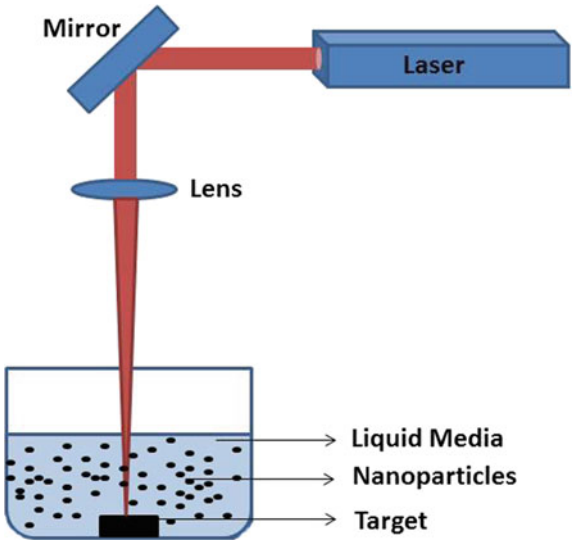

Fig. 1 Experimental setup for the LP-PLA technique

out with high kinetic energy. These intermediate species in the plume collide and react with molecules of the surrounding liquid, thus resulting in the formation of new compounds containing atoms from both the target and the liquid. Focusing of a high-power laser beam in nanosecond time scales results in the instantaneous increase in temperatures and pressures (many thousands of K at tens of GPa) within the reaction volume. LP-PLA technique which creates high-temperature, high-pressure and high-density conditions in a localized area thus leads to the formation of novel materials impossible by other conventional techniques. The experimental arrangement for the synthesis of nanostructures by LP-PLA techniques is shown in Fig. 1. The necessary condition for the formation of nanoparticles under ablation in liquid environment is the melting of the solids which occur at adequately high laser fluence relying upon the absorption efficiency of the material at the laser wavelength.

During the past decades, extensive research studies were performed in the formation of nanoparticles (NPs) employing laser ablation of solids, either in gas or in vacuum. This process of pulsed laser ablation can be controlled by understanding the mechanisms of cluster formations, and this technique is now being widely used for the growth of a large variety of compounds. LP-PLA can be considered as the extension of this concept. In both laser ablations in vacuum and at the solid–liquid interface, the interaction of laser beam with the target material is the same. Also, plasma will be produced in both types of laser ablation process and during the ablation; a strong confinement of ejected particles will be created as a result of electron–ion recombination. But the difference is that, for normal PLA the expansion of plasma occurs freely in vacuum, whereas in LP-PLA process, the plasma is confined by a liquid layer. Additionally, the presence of liquid layer delays the expansion of plasma, creating a high plasma pressure and temperature leading to the formation of novel materials. Another favorable aspect of LP-PLA process is that

the final product may contain the atoms of the solid target material and the liquid, as both are vaporized during the LP-PLA process. LP-PLA is a flexible and versatile technique for the synthesis of various novel nanoparticles and can be considered as a substitute to the well-known chemical vapor deposition (CVD) method. Besides, the generation of NPs through laser ablation of solid targets in liquid environment avoids surface functionalization and formation of counter-ions or surface-active substances [29, 30]. Thus, this LP-PLA offers the advantages of both pulsed laser deposition (PLD) and other chemical routes. The colloidal dispersion of nanoparticles obtained during LP-PLA process is found to more stable than that prepared by other chemical methods. In addition, the materials with complex stoichiometries can be grown by ablation process very easily. Moreover, materials which can only be synthesized at high pressure can also be grown by pulsed laser ablation in a liquid medium. Briefly, the material will be ejected and evaporated upon irradiating the target with high power over 0.1 GW/cm^2. A maximum pressure of several GPa generated by shock waves will be obtained with a laser power density of several GW/cm^2 [31]. But processes involved in the nucleation and transition of nanosystems in the LP-PLA technique are not clear. Some of the nucleation thermodynamics, the phase transition and the growth kinetics of nanocrystals by laser ablation of liquids are given by Yang [32].

Generally, LP-PLA is regarded as a quick and far-from-equilibrium process. In this process, the final product may contain all stable and metastable phases formed during the different stages of bulk to nanoparticle transition, especially for any metastable intermediate phases [32, 33]. Specifically, in LP-PLA process, the quenching time is very short so that the metastable intermediate phases which form during the transition from bulk to nanoparticle conversion can be frozen in, and final products will be formed. Berthe and co-workers [34] have mentioned that species ejected from the solid target surface have a large initial kinetic energy during the very initial stage of interaction of the high-energy laser with the solid–liquid interface. Due to the covering effect in the vicinity of the solid–liquid interface, the ejected species will form a dense region. This stage is similar to that of laser-generated plasma plume in vacuum or low-pressure gas. The plasma expands adiabatically at supersonic velocity leads to a shock wave in front of it as the plasma created in LP-PLA process is confined in the liquid. The shock wave thus generated will induce an extra, instantaneous pressure as it passes through the liquid. This laser-induced pressure will result in the increase in temperature in the plasma [35, 36]. Therefore, the plasma formed in LP-PLA is at higher pressure and higher density than that produced in PLA in gas or vacuum. The localized high temperature will also result in the vaporization of small amount of the surrounding liquid to form bubbles within the liquid. The bubbles will expand when more material is vaporized until at a certain combination of temperature and pressure, and finally, they will collapse. During the collapse of bubbles, the nearby species are subjected to temperatures of thousands of kelvin (K) and pressures of several gigapascal (GPa), and these extreme conditions result in the formation of novel materials [37].

LP-PLA has been used to produce nanoparticles (NPs) of many different metal elements including silicon [38, 39], titanium [40, 41], zinc [42, 43], cobalt [44, 45], silver [46, 47], copper [48, 49] and gold [50, 51]. This technique can also be used

to prepare NPs of compound materials such as TiC [52, 53], TiO_2 [54, 55] and CoO [44] in water and ZnSe and CdS in various solvents, including water [56–58]. The use of this method opens up the possibility of studying new materials at the nanoscale range for various new applications. LP-PLA has gained much attention recently for its ability to form more complex, higher-dimensional nanostructures, and a lot of research is going on the study of dynamical processes among laser–solid–liquid interactions. A summary of the nanostructures grown by LP-PLA technique is listed in Table 1.

The synthesis of various metal, semiconducting and ceramic nanostructures by LP-PLA techniques and their optical properties is discussed in the following sections.

Table 1 Summary of nanostructures grown by LP-PLA technique

Target	Medium	Laser source	Products	References
Ag	Water	Nd:YAG laser (532 nm)	Ag nanoparticles	[46]
Ag	Ethanol	Cu vapor laser (510.5 nm)	Ag nanoparticles	[52]
Au	Water	Nd:YAG laser (532 nm)	Au nanoparticles	[46]
Au	Alkane liquid	Nd:YAG laser (532 nm)	Au nanoparticles	[59]
Co	Water	Nd:YAG laser (355 nm)	Co_3O_4 nanoparticles	[44]
Hexagonal BN	Acetone	Nd:YAG laser (532 nm)	Cubic-BN nanoparticles	[60]
Graphite	Water	Nd:YAG laser (532 nm)	Diamond nanoparticles	[61]
Pt/TiO_2	Water	Nd:YAG laser (355 nm)	Pt/TiO_2 nanoparticles	[62]
Sn	Water + SDS	Nd:YAG laser (355 nm)	SnO_2 nanoparticles	[63]
Ti	Water + SDS	Nd:YAG laser (355 nm)	TiO_2 nanoparticles	[64]
Zn	Water + SDS	Nd:YAG laser (1064 nm)	ZnO nanoparticles	[65]
ZnO	Water	Nd:YAG laser (355 nm)	ZnO nanoparticles	[66]
ZnS	Water	Nd:YAG laser (266 nm)	ZnS nanoparticles	[67]

2 Metal Nanoparticles by LP-PLA Technique

The synthesis of noble metal nanoparticles such as silver, gold and copper by LP-PLA is widely studied, and the colloidal nanoparticles of these noble metals exhibit a very intense color, which is absent in the corresponding bulk counterpart as well as in the individual atoms. This coloration is due to the surface plasmon resonances (SPRs), and it is the collective oscillation of the free conduction electrons induced by the interacting electromagnetic fields [68]. This makes metal nanoparticles a prominent material for a wide range of applications, including nonlinear optical devices, biosensors, telecommunication and data storage [69, 70]. The size and shape of the nanoparticles play a key role in tuning its optical and electrical properties [71]. Several methods are available for controlling the size and shape of nanostructures and which include chemical reduction, ultrasonic reduction, and photolysis of salts [72, 73]. But these chemical reduction methods result in by-products that contaminate and affect the stability of the nanostructures. In this context, methods like laser ablation of solid target in liquid media have got considerable attention because of its safety and simplicity [74].

Mafune et al. explained the mechanism of nanoparticle growth during liquid phase-pulsed laser ablation [75], and according to this model, an electrical bilayer is formed around the nanoparticles, while the plume expands in the media like water [76]. In these media, the OH group on the nanoparticles generates surface charge and thus results in an electrical bilayer. The electrostatic repulsion between the charged nanoparticles prevents further growth and results in stable nanoparticles.

The nanoparticles of gold and silver with high quality can be synthesized by focusing second harmonics of a neodymium-doped yttrium aluminum garnet (Nd:YAG) laser (532 nm) operating at a repetition rate of 10 Hz onto a high-purity gold and silver target immersed in 15 mL of deionized water. The laser fluence dependence on the formation of these nanoparticles was studied by varying the fluences from 1.2 to 3.8 J/cm^2 with an ablation time of 1 h. The dependence of duration of laser ablation on the formation of nanoparticles has been investigated at particular laser fluence (1.2 J/cm^2), and concentrations of nanoparticles can be measured by inductively coupled plasma atomic emission spectroscopy (ICP-AES) analysis.

The UV-Vis absorption spectra will give information about the position of surface plasmon resonance in metal nanoparticles, and it can be monitored using JASCO V570 spectrophotometer in the wavelength region 200–1000 nm. Figure 2 shows the SPR peaks of gold and silver nanoparticles colloids prepared at 1.2 J/cm^2 which are in the visible region of the electromagnetic spectrum: 520 nm and 404 nm for gold and silver, respectively. According to Mie theory, a single SPR peak in the lower wavelength region for Au nanocrystals indicates the presence of spherically shaped Au nanocrystals which can be confirmed by TEM images. It is also found that the absorbance of the gold colloidal nanoparticles at a particular experimental condition is found to be smaller than silver nanoparticle colloids, and it indicates the increased concentration of the silver nanoparticles than the gold nanoparticles in water. This is due to the fact that ablation threshold is different for different materials since it

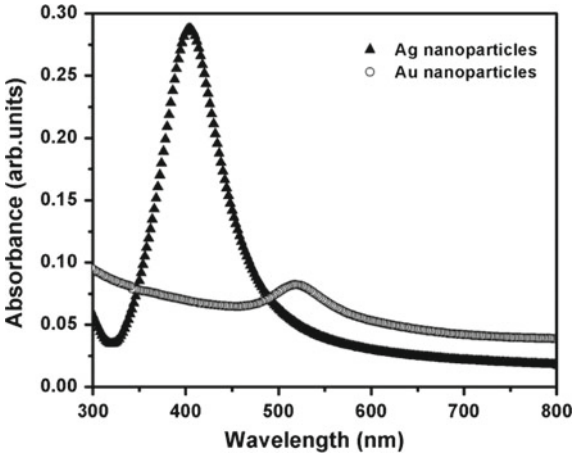

Fig. 2 The UV-Vis absorption spectra of silver and gold nanoparticles grown by LP-PLA technique at a laser fluence of 1.2 J/cm^2 for 1 h

depends upon the work function of the material. Work function may be defined as the minimum energy required for an electron to escape from the solid surface. For dragging an ion, out of the target electron requires an additional energy larger than or equal to the ion binding energy. Thus, the ablation threshold for metals is defined as the electron energy in the surface layer that must equal to the sum of atomic binding energy and work function. Assuming that during the laser–matter interaction process, the number density of the conducting electrons is unchanged and the condition to reach the ablation threshold is obtained as [77],

$$F_{\text{th}}^{\text{m}} \approx \frac{3}{8}(E_{\text{b}} + E_{\text{esc}})\frac{\lambda n_{\text{e}}}{2\pi} \tag{1}$$

where F_{th}^{m} is the threshold laser fluence for ablation of metal, E_{b} is the ion binding energy, E_{esc} is the work function, λ is the laser wavelength and n_{e} is the number density of the conduction electrons in the metal.

The work function of silver and gold is 3.7 eV and 4.7 eV, respectively, that results in higher ablation rate for silver than gold at particular laser fluence. ICP-AES analysis shows that the concentration of the silver and gold nanoparticles for a particular laser fluence is 3.8 ppm and 2.75 ppm, respectively, and it confirms the dependence of work function on the ablation rate of the metal targets.

Figure 3 shows the UV-Vis absorption spectra of gold nanoparticles prepared at different laser fluences varying from 1.2 to 3.8 J/cm^2. All the samples show a strong surface plasmon peaks only in the visible region (518–530 nm), and according to Mie theory, it is a property shown by spherical Au nanoparticles and it corresponds to the transverse mode of oscillation of the free electron cloud. Non-spherical particles, such as nanorods, exhibit an additional plasmon mode at higher wavelength (800 nm) and which correspond to the longitudinal mode of oscillation [78]. The absorption maxima of gold nanoparticles prepared at different laser fluencies show a redshift from 518 to 530 nm, and it indicates an increase in particle size [79]. For

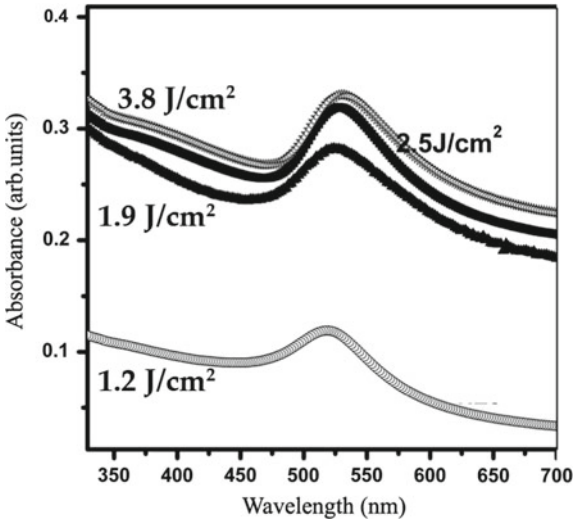

Fig. 3 UV-Vis absorption spectra of colloidal Au nanoparticles prepared at different laser fluences

larger particles, light cannot polarize the nanoparticles homogenously as the localization of the d band electrons in larger clusters increases the screening of the ions by surface electrons, thereby reducing the polarizability near the surface, and the retardation effect led to the excitation of higher-order modes [78]. This was regarded as an extrinsic size effect that results in redshift of SPR peak with an increase in nanoparticle size.

The amplitude of the SPR peak is found to increase with an increase in the ablation power, which can be attributed to the increased concentration of gold nanoparticles in water. The broadening in the SPR absorption band with decreasing particle size corresponds to the increased damping known as Landau damping [70]. There is no contribution to the observed broadening when the particles are apart, but when the volume fraction of the Au nanoparticles increased, an inter-particle interaction came into play.

Figure 4 shows the UV-Vis absorption spectra of silver nanoparticles grown at different laser fluences. The SPR bands peaking at 400 nm in the absorption spectra confirm the presence of nanosized silver particles. The plasmon band around 400 nm is attributed to the longitudinal surface plasmon resonance of the free electrons in the silver nanoparticles. A small shift from 403 to 406 nm is observed in the absorption peak with an increase in the ablation laser fluence, indicating only a small increase in the particle size which can be confirmed by TEM analysis (Fig. 6).

Transmission electron microscope (TEM) will tell about the size and shape of the synthesized metal nanoparticles and was performed with JEOL, TEM working at an accelerating voltage of 200 kV. For TEM measurements, the sample was prepared by drop-casting a drop of the colloidal nanoparticle solution onto a regular carbon-coated copper grid. Figure 5 shows the TEM, high-resolution transmission electron microscopy (HRTEM), selected area electron diffraction (SAED) patterns and size

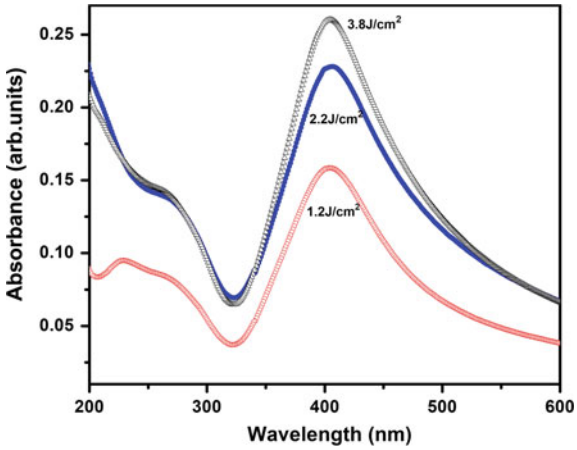

Fig. 4 UV-Vis absorption spectra of silver nanoparticles prepared at different laser fluences

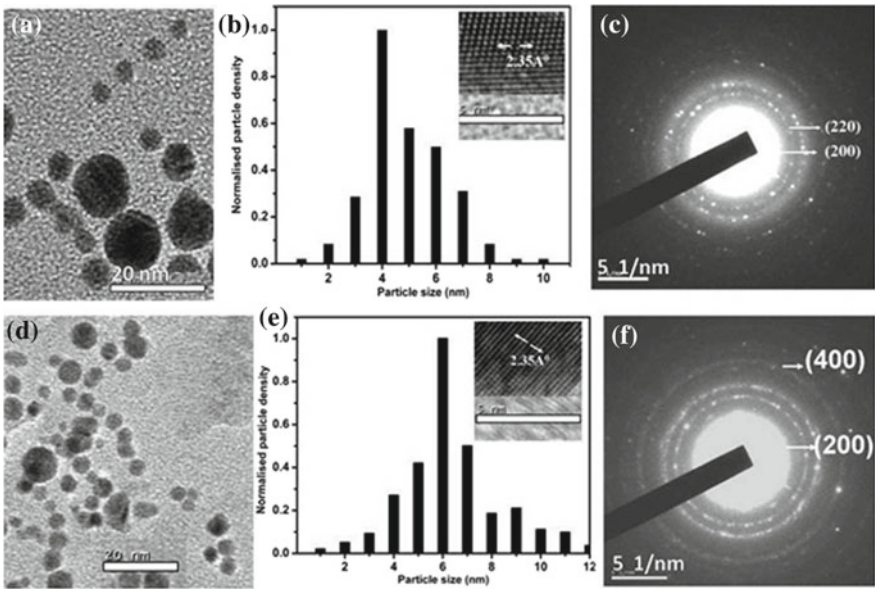

Fig. 5 **a** and **d** TEM, **b** and **e** size histograms, inset of **b** and **e** HRTEM, **c** and **f** SAED patterns of Au nanoparticles prepared at 1.2 (top row) and 3.8 J/cm^2 (bottom row)

histograms of gold nanoparticles grown at 1.2 and 3.8 J/cm^2. TEM image confirms the formation of uniformly distributed spherical gold nanoparticles in the aqueous media, as observed in the UV-Vis absorption spectra. The average particle sizes of the Au nanoparticles are 4 and 6 nm for 1.2 and 3.8 J/cm^2, respectively. The *d*-spacing values obtained from the SAED pattern are well-indexed and matches with

the (220), (200) and (400) planes of gold. The HRTEM displays the atomic planes corresponding to the (111) plane of gold with *d*-spacing of 2.35 Å.

Figure 6a and b shows the HRTEM image and SAED pattern of Ag nanoparticles grown at 1.2 J/cm^2. Similarly, Fig. 6c and d shows the HRTEM image and SAED pattern of silver nanoparticles grown at 3.8 J/cm^2. Inset of (b) and (d) shows high-resolution image showing parallel lines of atoms of silver. The *d*-values from high-resolution images and corresponding SAED pattern match with various planes of Ag. The nanoparticles grown at fluences 1.2 J/cm^2 and 3.8 J/cm^2 have an average size of about 4 nm and 7 nm, respectively.

The ICP-AES analysis shows that the concentration of the Au in the colloidal solution increases with an increase in the duration of laser ablation. Au nanoparticles of different concentrations such as 3.45, 4.25 and 7.65 ppm were synthesized at laser ablation durations of 1, 2 and 3 h, respectively. Presence of Au-NPs was confirmed

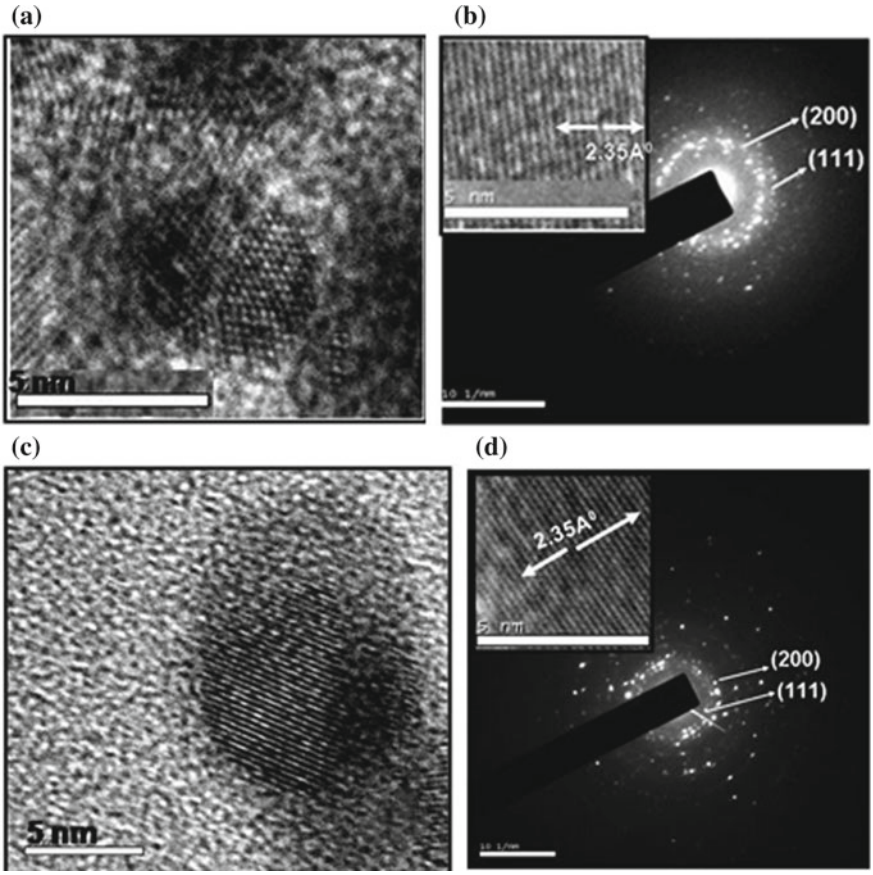

Fig. 6 HRTEM of Ag nanoparticles grown at a laser fluence of **a** 1.2 J/cm^2 and **c** 3.8 J/cm^2. **b** and **d** represent the SAED pattern of Ag nanoparticles (inset shows the parallel lines of atoms)

from the UV-Vis absorption spectra (Fig. 7), showing strong SPR peak at 520 nm. It was observed that with an increase in the duration of laser ablation, a gentle increase in the amplitude of the SPR peak is also visible. This corresponds to the increase in the concentration of the Au nanoparticles in the colloidal solution as noticed from the ICP-AES analysis. The plasmon peak remains at almost same wavelength owing to the fact that the particle size remains consistent with duration of laser ablation.

Figure 8 shows the UV-Vis absorption spectra of Ag nanoparticles grown at different duration of ablation by keeping particular laser fluence. Similar to gold nanoparticles, here also the amplitude of SPR peak is increasing with an increase in the duration of laser ablation and it is attributed to the increase in number of silver nanoparticles in water. It also shows that the SPR peak has a blue shift with an increase in the

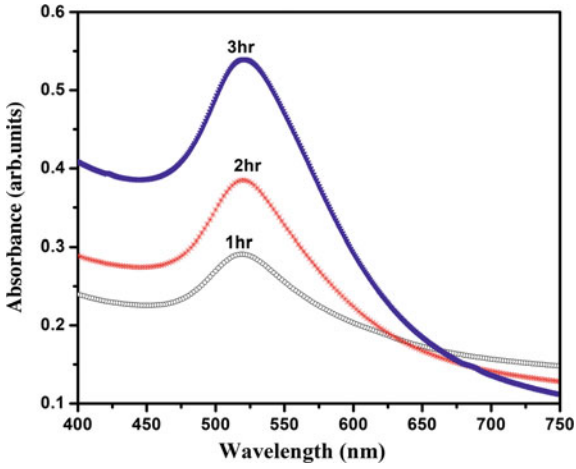

Fig. 7 UV-Vis absorption spectra of Au nanoparticles grown at various duration of ablation

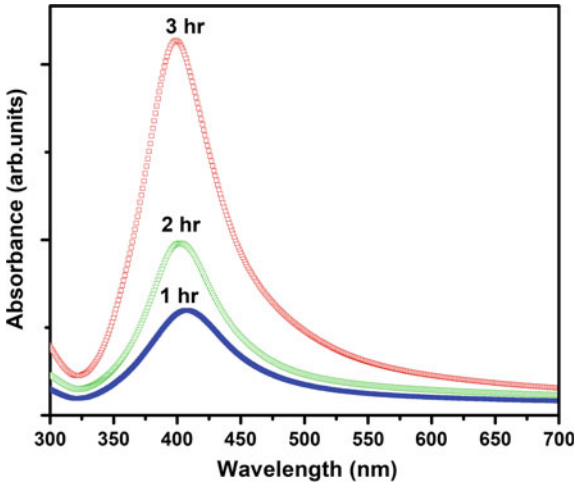

Fig. 8 UV-Vis absorption spectra of silver nanoparticles grown at a laser fluence of 1.2 J/cm^2 for different durations of ablation

duration of laser ablation, and it corresponds to the reduction in particle size due to the efficient radiation absorption by the previously ablated particles [80].

3 Semiconducting Nanoparticles by LP-PLA

ZnO nanoparticles were synthesized by employing a mosaic target of ZnO (99.99%) sintered at 1000 °C for 5 h. The target material was immersed in 15 mL of the liquid media with different pH and was irradiated by third harmonic of Nd:YAG laser (355 nm, repetition frequency of 10 Hz, pulse duration of 9 ns) at room temperature. A lens was used to focus the laser beam, and the ablation was done at a laser fluence of 15 mJ/ pulse. The spot size of the laser beam is about 1 mm. The duration of ablation was kept constant at 1 h. As a result, highly transparent dispersions of ZnO nanoparticles in liquid media were prepared by this simple LP-PLA technique at room temperature.

Transmission electron microscop e (JEOL, TEM) working at an accelerating voltage of 200 kV was used to confirm the formation of ZnO NPs. The sample for TEM was prepared by dropping ZnO nanoparticle colloidal solution onto standard carbon-coated copper grids and dried before recording the micrographs. TEM studies confirm the resulting product after laser ablation in different media contains particles in the nanoregime. The concentric rings in selective area electron diffraction (SAED) pattern correspond to formation of hexagonal ZnO. The result clearly proves the formation of crystalline ZnO NPs, and the formation of molecules like $Zn(OH)_2$ or ZnO/Zn core shell was not observed from these studies. The formation of ZnO constitutes the reaction of ejected molten material from the target with ambient medium at the outer surface [81]. Thereafter, the ejected plasma gradually cools down resulting in the formation of ZnO itself. The nanoparticles will be charged because there are many surface oxygen deficiencies. Since the isoelectronic points of ZnO (~9.3) are well above the pH (7.0) of pure water, it is observed that the as-grown ZnO nanoparticles by LP-PLA in pure water are normally charged [82]. As a result, this surface charge prevents the further aggregation, forming self-stabilized nanoparticles even in the absence of surfactant. Oxygen deficiency in the ZnO NPs synthesized by LP-PLA will also lead to positive charge which may prevent from agglomeration. It is found that there is a linear increase in the mean size of the particle with fluence of the laser pulses and is shown in Fig. 9.

However, higher laser fluence results in generation of bigger size particles with broad size distribution. Whereas, when the duration of ablation was increased maintaining lower fluence, the size of the NPs did not increase, but resulted in the increase in the particle density. But, even for ablation duration of more than 3 h at a laser energy of 45 mJ/pulse, the transparency of the ZnO nanoparticle colloid remained as such. While maintaining transparency, a maximum concentration of 17.5 μg/mL was obtained for ZnO nanoparticles [66].

Figure 10a details the TEM image of ZnO samples after laser irradiation with energy 25 mJ/pulse in the water (pH ~ 7). The observation indicates the formation

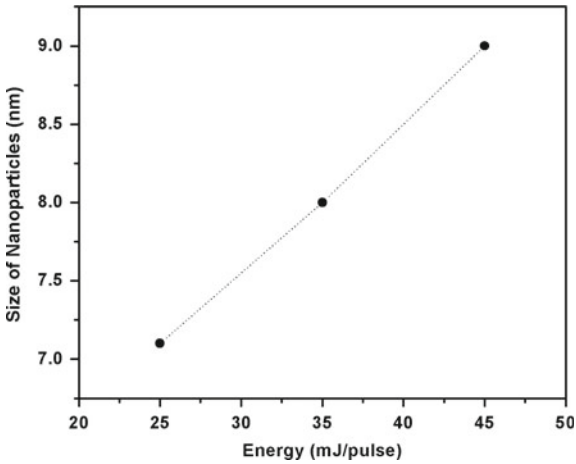

Fig. 9 Variation of size of the LP-PLA grown ZnO NPs with laser fluence [83]

of ZnO particles in the nanoregime. The particle size distribution of ZnO NPs was observed in a small range (Fig. 10b), and most of the particles are prone to have size of 7 nm. The HRTEM image (Fig. 10d) with inter-planar *d*-spacing value of 0.26 nm corresponds to the (002) plane of wurtzite ZnO. The particle size distribution was found to be nearly uniform. The selective area electron diffraction (SAED) pattern (Fig. 10c) displays sharp concentric rings corresponding to (100), (002), (102), (110) and (103) diffraction planes of hexagonal ZnO. Apparently, the results confirm the formation of crystalline ZnO NPs exhibiting random orientations. The high-resolution TEM image (inset Fig. 10d) clearly depicts the formation of ZnO NPs having hexagonal shape and the stacking of about 85 hexagonal unit cells makes 7-nm-sized NPs.

The TEM image shows that the particles are in spherical shape and it has an average size about 7 nm and the colloid is transparent in nature. The average particle size of Zn/ZnO composite nanoparticles grown by Zeng et al. [84] was 18 nm, and it was colored due to turbidity. Also, the ZnO NPs grown under oxygen bubbling into the water during laser ablation of ZnO targets are found to exhibit bigger size, while the size of the particles remains the same during nitrogen bubbling into water which is same as that grown in pure water. TEM images of the ZnO NPs grown in both oxygen and nitrogen atmosphere are shown in Fig. 11a. Figure 11b and c clearly shows that the NPs prepared in nitrogen atmosphere, keeping the other parameters of the experiment fixed have same size as those prepared in neutral water. But the oxygen bubbling during the ablation process results in increased amount of dissolved oxygen and promotes the growth of ZnO. This results in bigger ZnO NPs, whereas nitrogen bubbling in the solution during the LP-PLA process does not create any additional oxygen other than that produced by the laser interaction with the ZnO target. As a result, it is observed that the size of the particles remains the same as those obtained by LP-PLA in pure water.

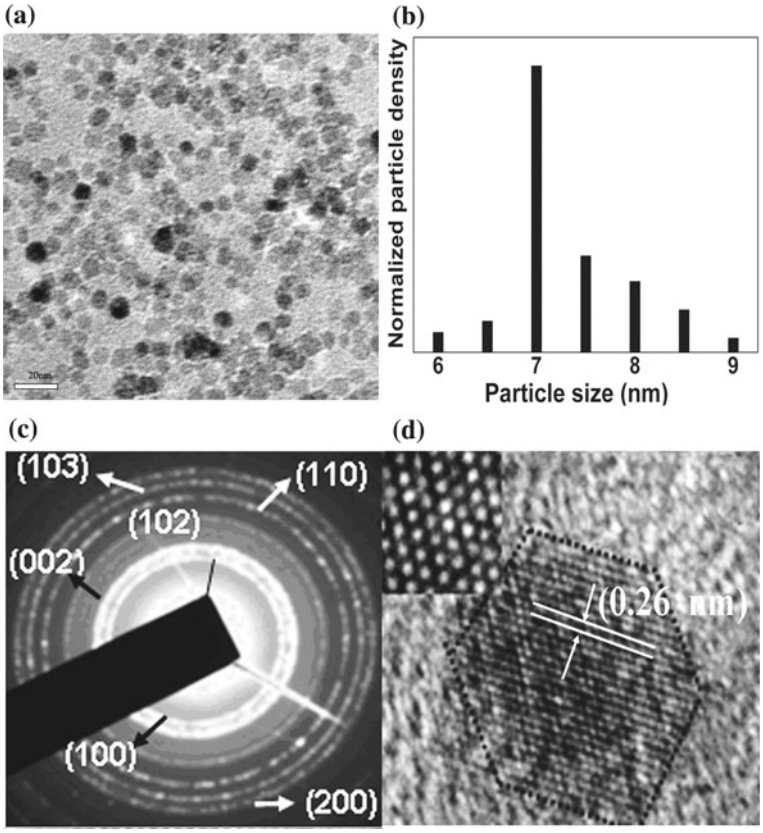

Fig. 10 **a** TEM image of ZnO NPs; **b** histogram representing size distribution; **c** SAED patterns matching hexagonal ZnO NPs prepared by LP-PLA technique with a fluence of 25 mJ/pulse in water. **d** HRTEM image for a single ZnO nanoparticle showing (002) crystalline plane and inset shows the stacking in hexagonal close-packed mode [66]

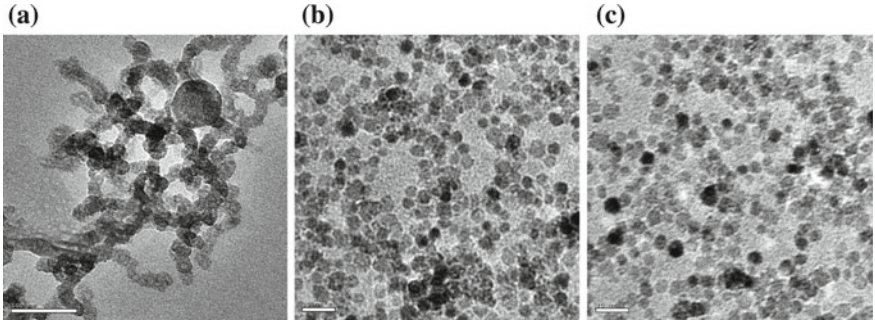

Fig. 11 TEM image of zinc oxide NPs grown by LP-PLA in water **a** oxygen atmosphere; **b** with nitrogen atmosphere and **c** without any gases [83]

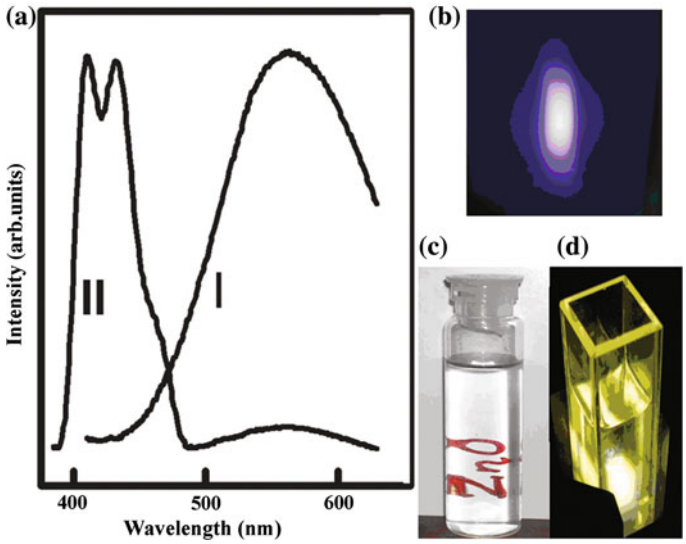

Fig. 12 **a** PL emission spectra of ZnO NPs grown without (curve I) and with (curve II) oxygen atmosphere at an excitation wavelength of 345 nm. **c** The photograph of synthesized transparent ZnO NPs and **d** its yellow PL emission under UV excitation. **b** The bluish-violet PL from the NPs grown in oxygen atmosphere [66]

Photoluminescence (PL) spectra were recorded using Jobin Yvon Fluoromax-3 spectrometer equipped with xenon lamp (150 W). PL measurement of NPs dispersed in neutral media was performed at an excitation wavelength of 345 nm. It was observed that the ZnO NPs dispersed in water show deep yellow luminescence as shown in Fig. 12. Figure 12c clearly pictures the photograph of ZnO NPs dispersed in water, which is highly transparent and its yellow emission under UV excitation (Fig. 12d). The origin of this yellow luminescence can be associated with the native oxygen defects [66] of the as-prepared ZnO NPs.

Oxygen bubbling experiment into the water during laser ablation of ZnO target was carried out to further confirm the origin of yellow luminescence due to oxygen vacancy. Bubbling of oxygen into water during laser ablation is found to suppress the yellow emission, resulting in PL emissions at 408 nm and 427 nm in the violet-blue region as shown in Fig. 12a (curve II). Photographic image displaying the deep bluish-violet emission is shown in Fig. 12b. The defect density was considerably reduced tending to more stoichiometric ZnO NPs due to the bubbling of oxygen into water during ablation, whereas the ZnO NPs grown under nitrogen atmosphere has similar size and PL emission characteristic as of those grown in neutral water without any gas bubbling. According to Lin et al. [85], the energy interval from valence band to zinc interstitials is found to be 2.9 eV. The PL emission at 427 nm for the ZnO NPs is very well consistent with these results. The weak Raman peak of the solvent corresponding to OH vibration was not detected in the PL spectra mainly because the PL emission intensity was very intense.

The ZnO NPs grown by LP-PLA method do not exhibit any green emission. However, the origin of green emission is still debatable. Nevertheless, there is strong evidence that it is presumably located at the surface [86]. And the absence of green PL emission proposes the desirable presence of $Zn(OH)_2$ on the surface of ZnO NPs grown through LP-PLA technique [87].

The growth mechanism of ZnO NPs by LP-PLA can be modeled as follows. The plasma on interaction of the laser beam with the ZnO target consisting of ionic and neutral species of Zn and oxygen [88] along with water vapor produced at the solid–liquid interface. High temperature (10^4–10^5 K) and pressure of few GPa [34] in the volume are produced due to the high intensity of the laser beam in the nanosecond scales. The adiabatic expansion of high-temperature plasma leads to the formation of ZnO which further interacts with the solvent water creating a thin layer of $Zn(OH)_2$ as ZnO is highly sensitive to H_2O environment [89]. As a result, a thin passivation layer of $Zn(OH)_2$ will be formed in ZnO NPs grown by LP-PLA in water. And the increase in the amount of dissolved oxygen due to oxygen bubbling into the water during the ablation process is found to promote the growth of ZnO NPs. This leads to the formation of bigger sized ZnO NPs. However, nitrogen bubbling into water does not make any extra oxygen other than that in the plasma produced by the laser interaction with the ZnO target. Hence, the particle size remains the same as those observed by LP-PLA in pure water.

Figure 13a shows the high-resolution transmission electron microscopic (HRTEM) image of the ZnO samples grown in acid media (pH ~ 5). The particles that have an elliptical shape with 15 nm size in the elongated region and 11 nm in the compressed region are observed from the HRTEM image. The SAED pattern (Fig. 13b) of the ZnO NPs prepared in acid media keeping all other experimental

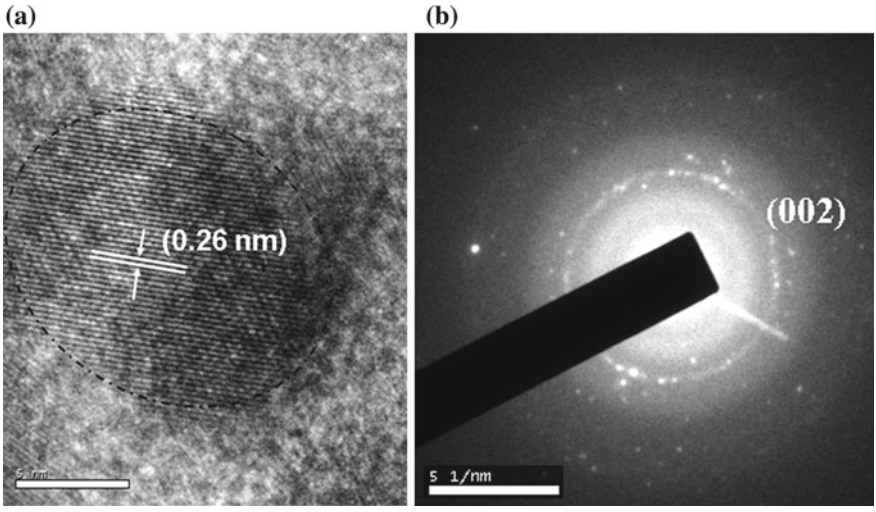

Fig. 13 **a** HRTEM image and **b** SAED pattern of ZnO NPs synthesized in acid media by LP-PLA method [83]

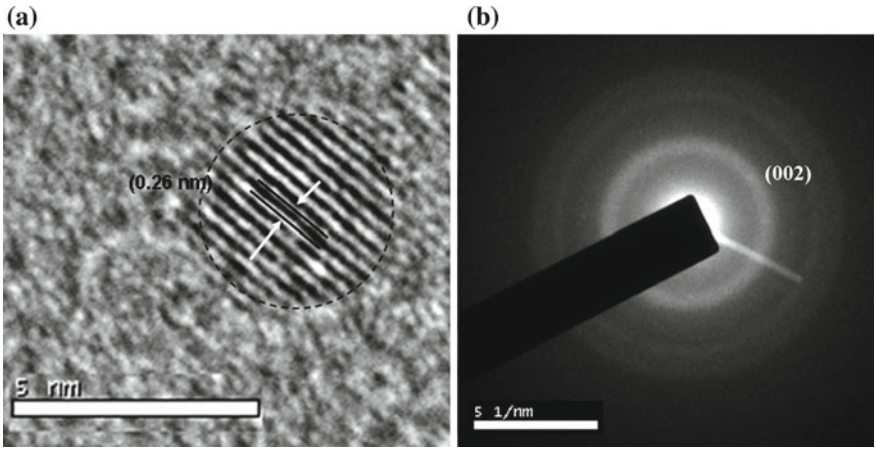

Fig. 14 **a** HRTEM image and **b** SAED pattern of ZnO NPs synthesized in basic media by LP-PLA method

parameters the same shows a ring pattern corresponding to the (002) plane of the wurtzite ZnO.

HRTEM and the SAED pattern of ZnO NPs prepared by pulsed laser ablation in basic media (pH ~ 9) are shown in Fig. 14a and b. Spherical particles having a size of about 4 nm were observed in the HRTEM image (Fig. 14a). SAED ring pattern indicates the (002) plane corresponding to the wurtzite ZnO. Altogether, these characterization results confirmed the formation of crystalline ZnO NPs by pulsed laser ablation in liquids.

The size of the ZnO NPs grown by LP-PLA in the acidic medium (pH = 5) shows relatively bigger than that synthesized in pure water under identical experimental conditions. Due to the higher dissolution rate of hydroxide in acidic medium, the formation of thin passivation layer of $Zn(OH)_2$ on the surface of the ZnO NPs during the cooling of laser plasma interacting with the liquid medium may be slower, thus favoring the formation of larger sized ZnO NPs. Whereas, the size of the ZnO NPs grown by ablation in alkali medium is smaller because the growth of $Zn(OH)_2$ is being favored by providing hydroxyl groups in the alkali medium. Thus, in conclusion, the thermodynamic conditions formed by the laser ablation plume in the liquid are localized to a nanometer regime which is not affected by the pH of the medium. Bigger sized NPs are formed with the increase in the energy of the laser beam due to ablation of large quantity of the material. The formation of hydroxide passivation layer is greatly determined by the pH of the solution which further alters the growth and size of the particles. As observed in the case of ablation of zinc metal targets in aqueous solution, no agglomeration of the particles was observed with the particles grown in neutral, acidic and alkaline media. Rather these particles were found to be well dispersed [90]. However, in the present study oxygen bubbling into water leads to the formation of bigger sized particles and agglomeration. As a result, the studies

suggest that the surface charge of ZnO NPs is mainly due to oxygen deficiency and less pronounced effect from pH of the medium.

4 Ceramic Nanoparticles by LP-PLA Technique

Optical imaging [91] is a powerful technique for imaging tissues or intracellular structures than magnetic resonance imaging [92] and radioactive molecular imaging (MRI) [93] because of its advantages such as low cost, high sensitivity and easy manipulation. The commonly used probes in optical imaging are fluorescent organic molecules and the other fluorescent nanoparticles. Traditional fluorescent dyes have limitations such as low fluorescence intensity and low photostability for using it as labeling agents [94].

There has been research interest in various luminescent semiconducting nanoparticles of CdSe, CdS, ZnS, InP, InAs, etc. as biological probes in diagnostic or targeted therapeutic applications. But many of these quantum dots are not suitable for medical application because of the presence of toxic materials such as cadmium or selenium, poor solubility and disposal issues. In this context, research has progressed to synthesize more suitable materials for medical and various biological applications. Researcher's main challenge is to develop a nanometer sized, highly biocompatible and biodegradable luminescent material for in-vivo imaging of human cells. Hydroxyapatite (HAp, $Ca_{10}(PO_4)_6(OH)_2$) is a typical green natural material because calcium phosphate is the inorganic mineral in bone and teeth. Lanthanide ions such as europium and terbium have interesting luminescence properties and which can be utilized for biological applications [95]. These rare-earth-doped materials exhibit narrow emission bands, and the emission color depends only on the dopant and doping concentration of lanthanide ions and not on the particle size. As pure hydroxyapatite is not able to exhibit substantial photoluminescence emissions, there is an ongoing research interest in the development of fluorescent lanthanide-doped hydroxyapatite which will demonstrate as promising materials for biomedical applications such as detection of tumor cells and as drug delivery vehicle to target tumor tissues or cells [96].

Nanoparticles of europium-doped HAp can be easily synthesized by the LP-PLA technique, and these nanoparticles emit light under UV and visible excitations. Fluorescent nanoparticles with visible excitation are ideal candidates for imaging of living cells. Pulsed laser ablation of a europium-doped HAp target immersed in 15 ml of water results in fluorescent HAp nanoparticles. Third harmonic of Nd-YAG laser (355 nm) with a repetition rate of 10 Hz is used for the LP-PLA experiment. Laser beam is focused on the target by using lens with a focal length of 20 cm. The target position was fixed at a position just before the focal point of the lens in order to avoid the pitting of target surface. The dependence of various processing parameters such as laser fluence, duration of ablation and the europium concentration on the properties of nanoparticles can be studied.

HRTEM image of the Eu-doped HAp sample shown in Fig. 15 confirms the formation of spherically shaped nanoparticles, and the average size of the nanoparticles is about 13 nm. The crystalline nature of the Eu-doped HAp nanoparticles is observed from the selected area electron diffraction (SAED) pattern, and the ring pattern corresponds to various planes of monoclinic structure of hydroxyapatite.

The dependence of laser fluence on the luminescence emission is studied by varying laser fluence from 1.9 to 5.7 J/cm^2. The variation of luminescence intensity with laser fluence is shown in Fig. 16. Eu-doped HAp nanoparticles exhibit PL emissions at 531, 572, 601 and 627 nm with an excitation wavelength of 325 nm. These emissions are originated from electronic transitions within the f-subshell and are assigned to ^5D_j–^7F_j transitions that are parity forbidden [97] by the Laporte selection rule. The emission line at 531, 572, 601 and 627 nm corresponds to $^5D_1$–$^7F_0$, $^5D_0$–$^7F_0$, $^5D_0$–$^7F_1$ and $^5D_0$–$^7F_2$ transition, respectively. This PL emission from the nanoparticles confirms the inclusion of europium in the HAp host lattice. These luminescence transition levels are due to the spin–orbit coupling of six electrons in the f-subshell, and the transitions are assigned to the mixing of odd terms due to the crystal field [98]. Unlike other Eu^{3+} phosphors, the PL peak corresponds to $^5D_0$–$^7F_0$ transition centered at 572 nm which is found to be stronger than that of $^5D_0$–$^7F_{1,2}$ transitions. It is also found that luminescence intensity increases with laser fluence (inset of Fig. 16) and is attributed to the increase in the production of nanoparticles.

The dependence of duration of ablation on the intensity of emission is also studied, and it is shown in Fig. 17. Here, the luminescent intensity decreases with duration of ablation, and it is shown in the inset of the figure. The nanoparticles formed during the LP-PLA process may absorb the incident photon energy leading to secondary processes such as heating/melting and welding/sintering and result in larger particles for longer duration of ablation [99]. The decrease in luminescence intensity with the increase in laser ablation time from 1 to 4 h is due to the increase in the particle size

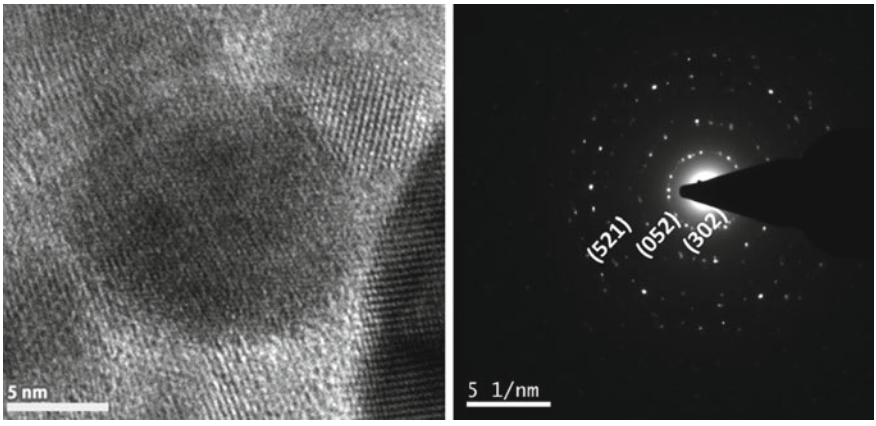

Fig. 15 HRTEM image (left) and SAED pattern (right) of Eu:HAp nanoparticles grown by LP-PLA technique

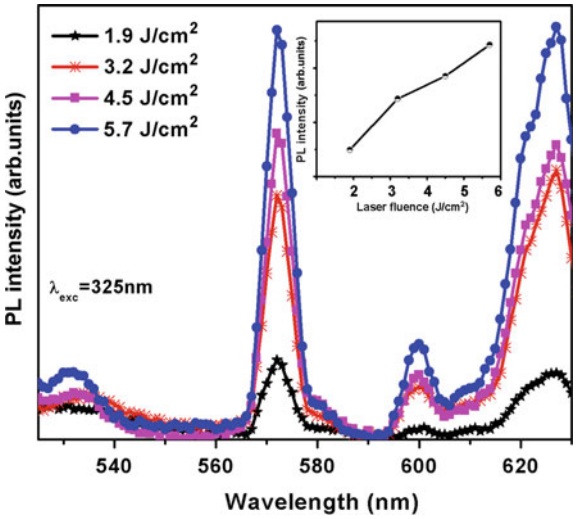

Fig. 16 PL emission spectra of Eu-doped HAp nanoparticles grown at different laser fluences. Inset shows the variation of PL intensity with laser fluence

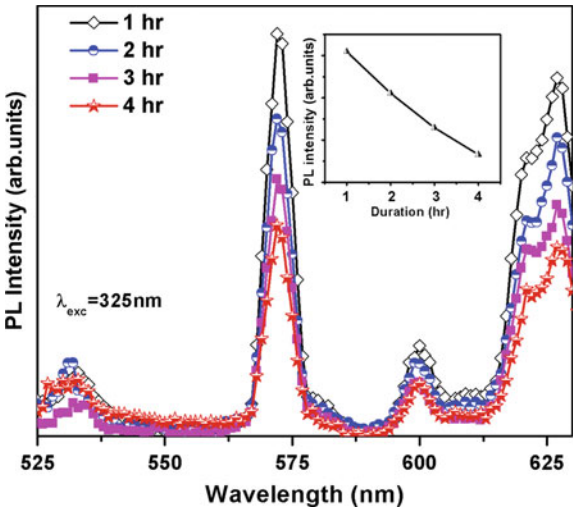

Fig. 17 PL spectra of Eu-doped HAp nanoparticles grown for different duration of ablation. Inset shows variation of PL intensity with duration of ablation

of the nanoparticles from 15 to 60 nm and which can be confirmed from the TEM images shown in Fig. 18.

Luminescent HAp nanoparticles with visible light excitation have applications in imaging of living cells for studying the change in situ at real time. Figure 19 (right)

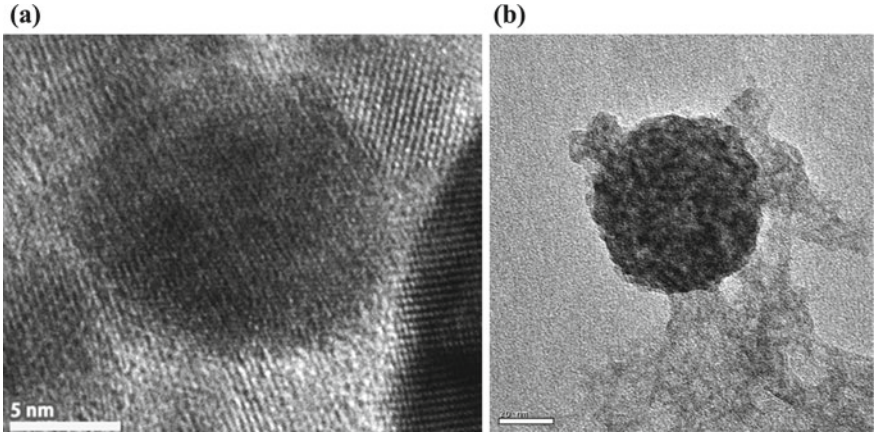

Fig. 18 TEM images of Eu-doped HAp nanoparticles grown at different duration of ablation. **a** 2 h and **b** 4 h

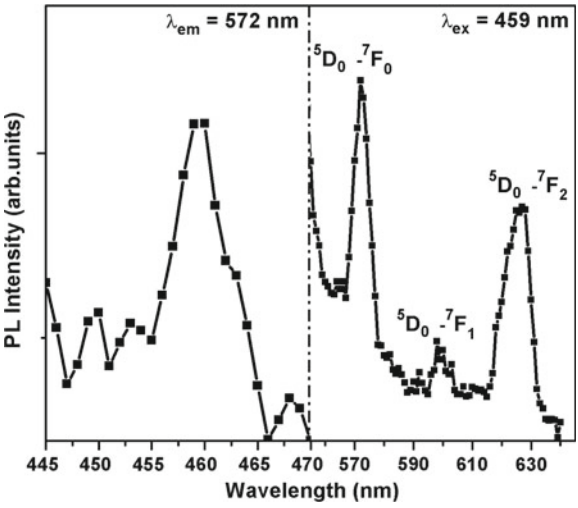

Fig. 19 Luminescence excitation (left) and emission (right) spectra under visible excitation of Eu-doped HAp nanoparticles

shows the PL spectra of Eu-doped HAp nanoparticles under visible excitation of 459 nm. It shows PL emissions at 572 nm, 601 nm and 627 nm and corresponds to the $^5D_0$–^7F_j (where $j = 0, 1, 2$) transitions of Eu^{3+} ion, respectively. A luminescence excitation spectrum monitored at emission wavelength 572 nm is shown in Fig. 19 (left). Excitation spectra showing a maximum at 459 nm correspond to the direct excitation of Eu^{3+} from the ground state to the higher level in the $4f^6$ configuration and can be assigned to $^7F_0$–$^5D_2$ transition.

5 Conclusions

Liquid phase-pulsed laser ablation (LP-PLA) is an excellent technique to synthesis nanoparticles of metals, semiconductors and ceramics without the addition of any surfactants. The properties of the particle can be modulated very easily by changing the parameters such as time of ablation, laser fluence, and pH of the medium. In summary, nanosized, chemically pure, gold (Au), silver (Ag), zinc oxide (ZnO) and europium (Eu^{3+})-doped Hydroxyapatite (HAp) nanoparticles were prepared through LP-PLA technique by varying the process parameters. The dependence of the work function on the ablation rate was explained using the example of LP-PLA of gold and silver nanoparticles. The ablation rate was found to increase with the decrease in work function. The size of the nanoparticles was found to increase with the increase of laser ablation fluence. The structural and luminescence properties of biocompatible ZnO and Eu^{3+}-doped HAp nanoparticles were studied in detail. These surfactant-free luminescent nanoparticles synthesized in water are ideal candidates for imaging of tumor cells and living cells and also for targeted drug delivery.

References

1. Yang PH, Sun X, Chiu J-F (2005) Transferrin-mediated gold nanoparticle cellular uptake. Bioconjugate Chem 16(3):494–496
2. Xueyi Z, Jianrong W, Gareth RW, Shiwei N, Qianqian Q, Li-Min Z (2019) Functionalized MoS_2-nanosheets for targeted drug delivery and chemo-photothermal therapy. Colloids Surf B 173(1):101–108
3. Gao X, Cui Y, Levenson M, Chung LWK, Nie S (2004) In vivo cancer targeting and imaging with semiconductor quantum dots. Nat Biotechnol 22(8):969–976
4. Chen J, Saeki F, Wiley BJ, Chang H, Cobb MJ, Li ZY, Au L, Zhang H, Kimmey MB, Li X, Xia Y (2005) Gold nanocages: bioconjugation and their potential use as optical imaging contrast agents. Nano Lett 5(3):473–477
5. Shengjie X, Dian L, Peiyi W (2015) One-pot, facile, and versatile synthesis of monolayer MoS_2/WS_2 quantum dots as bioimaging probes and efficient electrocatalysts for hydrogen evolution reaction. Adv Funct Mater 25(7):1127–1136
6. Kevin JM, Lihong J, Adam MB, Surangi J, Wen T, Mingyuan G, Robert L, Ana J (2018) Biocompatible semiconductor quantum dots as cancer imaging agents. Adv Mater 30(18):1706356 (1–18)
7. Brigger I, Dubernet C, Couvreur P (2002) Nanoparticles in cancer therapy and diagnosis. Adv Drug Deliv Rev 54(5):631–651
8. Chen J, Wiley B, Campbell D, Saeki F, Chang L, Au L, Lee J, Li X, Xia Y (2005) Gold nanocages: engineering their structure for biomedical applications. Adv Mater 17(18):2255–2261
9. Jeong-Eun P, Minho K, Jae-Ho H, Jwa-Min N (2017) Golden opportunities: plasmonic gold nanostructures for biomedical applications based on the second near-infrared window. Small Methods 1(3):1600032 (1–6)
10. Guanying C, Indrajit R, Chunhui Y, Paras NP (2016) Nanochemistry and nanomedicine for nanoparticle-based diagnostics and therapy. Chem Rev 116(5):2826–2885
11. Barcikowski S, Hustedt M, Chichkov BN (2008) Nanocomposite manufacturing using ultrashort-pulsed laser ablation in solvents and monomers. Polimery 53(9):657–662

12. Compagnini G, Scalisi AA, Puglisi O (2002) Ablation of Nobel metals on liquids: a method to obtain nanoparticles in a thin polymeric film. Phys Chem Chem Phys 4(12):2787–2791
13. Rybaltovskii AO, Buznik VM, Zavorotny YuS, Minaev NV, Timashev PS, Churbanov SN, Bagratashvili BN (2018) Synthesis of film nanocomposites under laser ablation and drift embedding of nanoparticles into polymer in supercritical carbon dioxide. Russ J Phys Chem B 12(7):1160–1165
14. Chacko L, Poyyakkara A, Kumar VBS, Aneesh PM (2018) MoS_2-ZnO nanocomposites as highly functional agents for anti-angiogenic and anti-cancer theranostics. J Mater Chem B. 6(19):3048–3057
15. Dijkkamp D, Venkatesan T, Wu XD, Shaheen SA, Jisrawi N, Minlee YH, Mclean WL, Croft M (1987) Preparation of Y-Ba-Cu oxide superconductor thin films using pulsed laser evaporation from high T_C bulk material. Appl Phys Lett 51(8):619–621
16. Silvia H, Kota H, Hikaru S, Hidenori H, Hideo H (2016) In-situ growth of superconducting $SmO_{1-x}F_xFeAs$ thin films by pulsed laser deposition. Sci Rep 6(35797):1–6
17. Pappas DL, Saenger KL, Bruley J, Krakow W, Cuomo JJ, Gu T, Collins RW (1992) Pulsed laser deposition of diamond-like carbon films. Appl Phys 71(11):5675
18. Cheng Y, Lu YM, Guo YL, Huang GJ, Wang SY, Tian FT (2017) Multilayers diamond-like carbon film with germanium buffer layers by pulsed laser deposition. Surf Rev Lett 24(02):1750014 (1–6)
19. Radhakrishnan G, Adams PM (1999) Pulsed-laser deposition of particulate-free TiC coatings for tribological applications. Appl Phys A 69(Suppl 1):S33–S38
20. Balakrishnan G, Elangovan T, Shin-Sung Y, Kim D-E, Kuppusami P, Venkatesh BR, Sastikumar D, Jungil S (2017) Microstructural and tribological studies of Al_2O_3/ZrO_2 nanomultilayer thin films prepared by pulsed laser deposition. Adv Mater Lett 8(4):410–417
21. Dureuil V, Ricolleau C, Gandais M, Grigis C, Lacharme JP, Naudon A (2001) Growth and morphology of cobalt nanoparticles on alumina. J Cryst Growth 233(4):737–748
22. Ayman MD, Wael HE, Ali AS, Mohamed HT (2015) Synthesis of nano-cadmium sulfide by pulsed laser ablation in liquid environment. Spectrosc Lett 48(9):638–645
23. Patil PP, Phase DM, Kulkarni SA, Ghaisas SV, Kulkarni SK, Kanetkar SM, Ogale SB, Bhide VG (1987) Pulsed-laser-induced reactive quenching at liquid–solid interface: aqueous oxidation of iron. Phys Rev Lett 58(3):238–241
24. Scherer GW (1985) Glasses and ceramics from colloids. J Non-Cryst Solids 73(1):661–667
25. Dahl JA, Maddux BL, Hutchison JE (2007) Towards greener nanosynthesis. Chem Rev 107(6):2228–2269
26. Hartmann S, Brandhuber D, Husing N (2007) Glycol-modified silanes: novel possibilities for the synthesis of hierarchically organized (hybrid) porous materials. Acc Chem Res 40(9):885–894
27. Mende S, Stenger F, Peukert W, Schwedes J (2004) Production of sub-micron particles by wet comminution in stirred media mills. J Mater Sci 39(16):5223–5226
28. Besner S, Kabashin AV, Winnik FM, Meunier M (2008) Ultrafast laser based "green" synthesis of non-toxic nanoparticles in aqueous solutions. Appl Phys A 93(4):955–959
29. Wang JB, Zhang CY, Zhong XL, Yang GW (2002) Cubic and hexagonal structures of diamond nanocrystals formed upon pulsed laser induced liquid–solid interfacial reaction. Chem Phys Lett 361(1–2):86–90
30. Suha IA, Adel KM, Zaineb FM (2015) Study the effect of different liquid media on the synthesis of alumina (Al_2O_3) nanoparticle by pulsed laser ablation technique. Manuf Sci Technol 3(4):77–81
31. Fabbro R, Fournier J, Ballard P, Devaux D, Virmont J (1990) Physical study of laser-produced plasma in confined geometry. J Appl Phys 68(2):775–784
32. Yang GW (2007) Laser ablation in liquids: applications in the synthesis of nanocrystals. Prog Mater Sci 52(4):648–698
33. Liu P, Cui H, Wang C, Yang GW (2010) From nanocrystal synthesis to functional nanostructure fabrication: laser ablation in liquid. Phys Chem Chem Phys 12(16):3942–3952

34. Berthe L, Fabbro R, Peyre P, Tollier L, Bartnicki E (1997) Shock waves from a water-confined laser-generated plasma. J Appl Phys 82(6):2826–2832
35. Zhu S, Lu YF, Hong MH (2001) Laser ablation of solid substrates in a water-confined environment. Appl Phys Lett 79(9):1396–1398
36. Zhu S, Lu YF, Hong MH, Chen XY (2001) Laser ablation of solid substrates in water and ambient air. J Appl Phys 89(4):2400–2403
37. Shaw SJ, Schiffers WP, Gentry TP, Emmony DC (1999) A study of the interaction of a laser-generated cavity with a nearby solid boundary. J Phys D 32(14):1612–1617
38. Takada N, Sasaki T, Sasaki K (2008) Synthesis of crystalline TiN and Si particles by laser ablation in liquid nitrogen. Appl Phys A 93(4):833–836
39. Rawat R, Tiwari A, Vendamani VS, Pathak AP, VenugopalRao S, Tripathi A (2018) Synthesis of Si/SiO_2 nanoparticles using nanosecond laser ablation of silicate-rich garnet in water. Opt Mater 75:350–356
40. Simakin AV, Voronov VV, Kirichenko NA, Shafeev GA (2004) Nanoparticles produced by laser ablation of solids in liquid environment. Appl Phys A 79(4):1127–1132
41. Anton AP, Gleb T, Noé D, Charlotte B, Khaled M, Nicola J, Al-Kattan A, Benoit L, Diane B, Serge M, Da Silva A, Marie-Anne E, Andrei VK (2019) Laser-synthesized TiN nanoparticles as promising plasmonic alternative for biomedical applications. Sci Rep 9(1):1194 (1–11)
42. Singh SC, Gopal R (2007) Zinc nanoparticles in solution by laser ablation technique. Bull Mater Sci 30(3):291–293
43. Neli M, Aljulaih AA, Wilfried W, Sergei AK, Satoru I (2018) Laser-ablated ZnO nanoparticles and their photocatalytic activity toward organic pollutants. Materials 11(7):1127 (1–11)
44. Tsuji T, Hamagami T, Kawamura T, Yamaki J, Tsuji M (2005) Laser ablation of cobalt and cobalt oxides in liquids: influence of solvent on composition of prepared nanoparticles. Appl Surf Sci 243(1–4):214–219
45. Borghei SM, Bakhtiyari F (2017) Study of the physical properties of cobalt/cobalt oxide particles synthesized by pulsed laser ablation in different liquid media. Acta Phys Pol A 131(3):332–335
46. Sreeja R, Reshmi R, Aneesh PM, Jayaraj MK (2012) Liquid phase pulsed laser ablation of metal nanoparticles for nonlinear optical applications. Sci Adv Mater 4(3–4):439–448
47. Dongshi Z, Wonsuk C, Jurij J, Mark-Robert K, Stephan B, Sung-Hak C, Koji S (2018) Spontaneous shape alteration and size separation of surfactant-free silver particles synthesized by laser ablation in acetone during long-period storage. Nanomaterials 8(7):529 (1–17)
48. Yeh MS, Yang YS, Lee YP, Lee HF, Yeh YH, Yeh CS (1999) Formation and characteristics of Cu colloids from CuO powder by laser irradiation in 2-propanol. J Phys Chem B 103(33):6851–6857
49. Marzun G, Bönnemann H, Lehmann C, Spliethoff B, Weidenthaler C, Barcikowski S (2017) Role of dissolved and molecular oxygen on Cu and PtCu alloy particle structure during laser ablation synthesis in liquids. Chemphyschem 18(9):1175–1184
50. Sylvestre JP, Poulin S, Kabashin AV, Sacher E, Meunier M, Luong JHT (2004) Surface chemistry of gold nanoparticles produced by laser ablation in aqueous media. J Phys Chem B 108(43):16864
51. Xiaoxia X, Lei G, Guotao D (2018) The fabrication of Au@C core/shell nanoparticles by laser ablation in solutions and their enhancements to a gas sensor. Micromachines 9(6):278 (1–13)
52. Dolgaev SI, Simakin AV, Voronov VV, Shafeev GA, Bozon-Verduraz F (2002) Nanoparticles produced by laser ablation of solids in liquid environment. Appl Surf Sci 186(1–4):546–551
53. De Bonis A, Santagata A, Galasso A, Laurita A, Teghil R (2017) Formation of titanium carbide (TiC) and TiC@C core–shell nanostructures by ultra-short laser ablation of titanium carbide and metallic titanium in liquid. J Colloid Interface Sci 489:76–84
54. Sugiyama M, Okazaki H, Koda S (2002) Size and shape transformation of TiO_2 nanoparticles by irradiation of 308-nm laser beam. Jpn J Appl Phys 41(7A):4666–4674
55. Wisam JA, Saja QA, Jassim NZ (2018) Production TiO_2 nanoparticles using laser ablation in ethanol. Silicon 10(5):2101–2107

56. Ankin KV, Melnik NN, Simakin AV, Shafeev GA, Voronov VV, Vitukhonovsky AG (2002) Formation of ZnSe and CdS quantum dots via laser ablation in liquids. Chem Phys Lett 366(3–4):357–360
57. Ismail RA, Hamoudi WK, Abbas HF (2018) New route for cadmium sulfide nanowires synthesis via pulsed laser ablation of cadmium in thiourea solution. Mater Res Express 5(2):025017 (1–26)
58. Xiao Y, Deng G, Feng G, Ning S, Wang S, Chen X, Yang H, Zhou S (2019) Femtosecond laser induced nano-meter size surface structures on ZnSe film. AIP Adv 9:015106 (1–6)
59. Compagnini G, Scalisi AA, Puglisi O (2003) Production of gold nanoparticles by laser ablation in liquid alkanes. J Appl Phys 94(12):7874–7877
60. Wang JB, Yang GW, Zhang CY, Zhong XL, Ren ZHA (2003) Cubic-BN nanocrystals synthesis by pulsed laser induced liquid–solid interfacial reaction. Chem Phys Lett 367(1–2):10–14
61. Yang L, May PW, Yin L, Smith JA, Rosser KN (2007) Growth of diamond nanocrystals by pulsed laser ablation of graphite in liquid. Diamond Relat Mater 16(4–7):725–729
62. Sasaki T, Liang C, Nichols WT, Shimizu Y, Koshizaki N (2004) Fabrication of oxide base nanostructures using pulsed laser ablation in aqueous solutions. Appl Phys A 79(4):1489–1492
63. Liang CH, Shimizu Y, Sasaki T, Koshizaki N (2003) Synthesis of ultrafine SnO_{2-x} nanocrystals by laser-induced reactive quenching in liquid medium. J Phys Chem B 107(35):9220–9225
64. Liang CH, Shimizu Y, Sasaki T, Koshizaki N (2005) Preparation of ultrafine TiO_2 nanocrystals via pulsed-laser ablation of titanium metal in surfactant solution. Appl Phys A 80(4):819–822
65. Zeng HB, Cai WP, Hu JL, Duan GT, Liu PS, Li Y (2006) Violet photoluminescence from shell layer of Zn/ZnO core–shell nanoparticles induced by laser ablation. Appl Phys Lett 88(17):171910 (1–3)
66. Ajimsha RS, Anoop G, Aravind A, Jayaraj MK (2008) Luminescence from surfactant-free Zno quantum dots prepared by laser ablation in liquid. Electrochem Solid-State Lett 11(2):K14–K17
67. Aneesh PM, Shijeesh MR, Aravind A, Jayaraj MK (2014) Highly luminescent undoped and Mn-doped Zns nanoparticles by liquid phase pulsed laser ablation. Appl Phys A: Mater Sci Process 116(3):1085–1089
68. Papavassiliou GC (1979) Optical properties of small inorganic and organic metal particle. Prog Solid State Chem 12(3–4):185–271
69. Festag G, Steinbruck A, Wolff A, Csaki A, Moller R, Fritzsche W (2005) Optimization of gold nanoparticle-based DNA detection for microarrays. J Fluoresc 15(2):161–170
70. Mishra YK, Mohapatra S, Avasthi DK, Kabiraj D, Lalla NP, Pivin JC, Sharma H, Kar R, Singh N (2007) Gold-silica nanocomposites for the detection of human ovarian cancer cells: a preliminary study. Nanotechnology 18(34):345606 (1–5)
71. Mulvaney P (1996) Surface plasmon spectroscopy of nanosized metal particles. Langmuir 12(3):788–800
72. Favier F, Walter EM, Zach MP, Benter T, Penner RM (2001) Hydrogen sensors and switches from electrodeposited palladium mesowire arrays. Science 293(5538):2227–2231
73. Hu J, Odom TW, Lieber CM (1999) Chemistry and physics in one dimension: synthesis and properties of nanowires and nanotubes. Acc Chem Res 32(5):435–445
74. Kabashin AV, Meunier M (2003) Synthesis of colloidal nanoparticles during femtosecond laser ablation of gold in water. J Appl Phys 94(12):7941–7943
75. Mafune F, Kohno JY, Takeda Y, Kondow T, Sawabe H (2000) Formation and size control of silver nanoparticles by laser ablation in aqueous solution. J Phys Chem B 104(39):9111–9117
76. Turkevich J, Stevenson PC, Hillier J (1951) A study of the nucleation and growth processes in the synthesis of colloidal gold. J Discuss Faraday Soc 11:55–75
77. Gamaly EG, Rode AV, Davies BL (2002) Ablation of solids by femtosecond lasers: ablation mechanism and ablation thresholds for metals and dielectrics. Phys Plasmas 9(9):949–957
78. Link S, El Sayed MA (2003) Optical properties and ultrafast dynamics of metallic nanocrystals. Annu Rev Phys Chem 54:331–366
79. Karthikeyan B, Thomas J, Philip R (2005) Optical nonlinearity in glass-embedded silver nanoclusters under ultrafast laser excitation. Chem Phys Lett 414(4):346–350

80. Tilaki RM, Irajizad A, Mahdavi SM (2006) Stability, size and optical properties of silver nanoparticles prepared by laser ablation in different carrier media. Appl Phys A 84(1):215–219
81. Nichols WT, Sasaki T, Koshizaki N (2006) Laser ablation of a platinum target in water: III. Laser induced reactions. J Appl Phys 100(11):114913 (1–7)
82. Kooli F, Chsem IC, Vucelic W, Jones W (1996) Synthesis and properties of terephthalate and benzoate in intercalates of Mg-Al layered double hydroxides possessing varying layer charge. Chem Mater 8(8):1969–1977
83. Aneesh PM, Aravind A, Reshmi R, Ajimsha RS, Jayaraj MK (2009) Dependence of size of liquid phase pulsed laser ablated ZnO nanoparticles on pH of the medium. Trans Mater Res Soc Jpn 34(4):759–763
84. Zeng HB, Cai WP, Li Y, Hu JL, Liu PS (2005) Composition/structural evolution and optical properties of ZnO/Zn nanoparticles by laser ablation in liquid media. J Phys Chem B 109(39):18260–18266
85. Lin BX, Fu ZX, Jia YB (2001) Green luminescent center in undoped zinc oxide films deposited on silicon substrates. Appl Phys Lett 79(7):943–945
86. Djurisic AB, Leung YH (2006) Optical properties of ZnO nanostructures. Small 2(8–9):944–961
87. Zhou H, Alves H, Hofmann DM, Kriegseis W, Meyer BK, Kaczmarczyk G, Hoffmann A (2002) Behind the weak excitonic emission of ZnO quantum dots: ZnO/$Zn(OH)_2$ core–shell structure. Appl Phys Lett 80(2):210–212
88. Joshy NV, Saji KJ, Jayaraj MK (2008) Spatial and temporal studies of laser ablated ZnO plasma. J Appl Phys 104(5):053307 (1–6)
89. Nakagawa M, Mitsudo H (1986) Anomalous temperature dependence of the electrical conductivity of zinc oxide thin films. Surf Sci 175(1):157–176
90. He C, Saski T, Usui H, Shimizu Y, Koshizaki N (2007) Fabrication of ZnO nanoparticles by pulsed laser ablation in aqueous media and pH-dependent particle size: an approach to study the mechanism of enhanced green photoluminescence. J Photochem Photobiol A: Chem 191(1):66–73
91. Weissleder R (2001) A clearer vision for in vivo imaging. Nat Biotechnol 19(4):316–317
92. Mahmoudi M, Hosseinkhani H, Hosseinkhani M, Boutry S, Simchi A, Journeay WS, Subramani K, Laurent S (2011) Magnetic resonance imaging tracking of stem cells in vivo using iron oxide nanoparticles as a tool for the advancement of clinical regenerative medicine. Chem Rev 111(2):253–280
93. Paulus MJ, Gleason SS, Easterly ME, Foltz CJ (2001) A review of high-resolution X-ray computed tomography and other imaging modalities for small animal research. Lab Anim 30(3):36–45
94. Zondervan R, Kulzer F, Kol'chenko MA, Orrit M (2004) Photobleaching of Rhodamine 6G in poly(vinyl alochol) at the ensemble and single-molecule levels. J Phys Chem A 108(10):1657–1665
95. Dosev D, Nichkova M, Kennedy IM (2008) Inorganic lanthanide nanophosphors in biotechnology. J Nanosci Nanotechnol 8(3):1052–1067
96. Yang C, Yang P, Wang W, Gai S, Wang J, Zhang M, Lin J (2009) Synthesis and characterization of Eu-doped hydroxyapatite through a microwave assisted microemulsion process. Solid State Sci 11(11):1923–1928
97. Chane-Ching JY, Lebugle A, Rousselot I, Pourpoint A, Pelle F (2007) Colloidal synthesis and characterization of monocrystalline apatite nanophosphors. J Mater Chem 17(28):2904–2913
98. Jagannathan R, Kottaisamy M (1995) Eu^{3+} luminescence: a spectral probe in $M_5(PO_4)_3X$ apatites (M = Ca or Sr; X = F^-, Cl^-, Br^- or OH^-). J Phys: Condens Mater 7(44):8453–8466
99. Yan Z, Chrisey DB (2012) Pulsed laser ablation in liquid for micro-/nanostructure generation. J Photochem Photobiol C 13(3):204–223